Applied Catalysis B: Environmental 225 (2018) 8–21

Contents lists available at ScienceDirect

Applied Catalysis B: Environmental

journal homepage: www.elsevier.com/locate/apcatb

Highly efficient photocatalytic activity and mechanism of Yb^{3+}/Tm^{3+} codoped In_2S_3 from ultraviolet to near infrared light towards chromium (VI) reduction and rhodamine B oxydative degradation

Zhibin Wu[a,b], Xingzhong Yuan[a,*], Guangming Zeng[a,b], Longbo Jiang[a,b], Hua Zhong[a,b], Yingcong Xie[a,b], Hui Wang[a,b], Xiaohong Chen[c], Hou Wang[a,b,d,*]

[a] College of Environmental Science and Engineering, Hunan University, Changsha, 410082, PR China
[b] Key Laboratory of Environment Biology and Pollution Control, Hunan University, Ministry of Education, Changsha, 410082, PR China
[c] Mobile E – business 2011 Collaborative Innovation Center of Hunan Province, Hunan University of Commerce, Changsha, 410205, China
[d] School of Chemical and Biomedical Engineering, Nanyang Technological University, Singapore, 637459, Singapore

ARTICLE INFO

Keywords:
Yb^{3+}/Tm^{3+} codoped In_2S_3
Photocatalysis
Full – spectrum
Chromium (VI) ; Rhodamine B

ABSTRACT

The Yb^{3+}/Tm^{3+} codoped flower – like tetragonal In_2S_3 photocatalysts were synthesized through a hydrothermal route, and the crystal phases, morphologies, chemical compositions and optical properties were characterized. The results shown that the doping with Yb^{3+}/Tm^{3+} did not significantly change the crystallinity of In_2S_3, but induced the generation of intermediate energy states for efficient charge separation. The Yb^{3+}/Tm^{3+} codoped In_2S_3 presented a significant enhancement of photoactivity towards chromium (VI) reduction and rhodamine B oxidation from UV to NIR light. The best photocatalytic synergism was obtained for the sample with the mole ratio of In^{3+}:Yb^{3+}:Tm^{3+} at 159:40:1, in which the chromium (VI) reduction efficiency was 97.9% (NIR, 100 min), 99.3% (vis, 10 min) and 98.3% (UV, 10 min), while the rhodamine B degradation efficiency was 98.4% (NIR, 100 min), 97.3% (vis, 14 min), and 96.3% (UV, 14 min). The favorable NIR photoactivity was mainly attributed to the upconversion mechanism via energy level transition of Yb^{3+}/Tm^{3+}. Under the full – spectra – light irradiation for 6 min and 7 min, the removal efficiency of chromium (VI) and rhodamine B could reach to 99.4% and 94.8%, the corresponding rate constant was 2.17 and 5.60 times of pure In_2S_3, respectively. The improved photocatalytic efficiency might be attributed to the enhanced light absorption and favorable charge separation resulted from the intermediate energy states and/or sulfur vacancies. In addition, the free radical capture and electron spin resonance experiments were also performed to determined the role of $\cdot O_2^-$ and h^+ species during photocatalytic oxidation process.

1. Introdution

Over the past decades, the increasing energy crisis and environmental pollution have become the restrictions in economic development worldwide [1–3]. Fortunately, semiconductor photocatalysis has attracted immense attention to overcome these problems, which can convert the solar energy for the clean energy production and pollutants decomposition [4–6]. As is known, the 50% of total solar energy that can reache the earth's surface is consisted of the ultraviolet (UV), visible and near–infrared (NIR) light in the proportion of ~ 5%, ~46% and ~49%, respectively [7–9]. However, most of conventional photocatalysts, such as TiO_2 [10,11], ZnO [12] and SnO_2 [13], etc., only can be excited by UV light to generate charge carriers for promoting the surface redox reactions, which is the gargantuan obstacle for the maximum utilization of solar energy.

For efficient solar energy conversion, the broad–spectrum responsive photocatalysts from UV to NIR wavelength have been the promising alternative [14,15]. To date, the $Cu_2(OH)PO_4$ [16], Bi_2MO_6 (M = W, Mo) [17,18], sulfides [19–21], birnessite [8,14], and C_3N_4 based [22], carbon quntum dots doped [23], plasmonic–enhanced [24], lanthanide doped [7,25,26] materials and so on have been exploited to utilize NIR light. Among them, the sulfides and the lanthanide doped nanoparticles have been considered to have the favarable application prospects [27]. The sulfides are the major group of abundant and cheap minerals, which have been demonstrated as visible and even NIR resonsive photocatalysts for environment remediation. In our previous studies, the $Co_{2.67}S_4$ nanoparticle with mixed valence state of Co^{2+}/Co^{3+} redox couple and Sb_2S_3/ultrathing–C_3N_4 sheets heterostructures

* Corresponding authors at: College of Environmental Science and Engineering, Hunan University, Changsha, 410082, PR China
E-mail addresses: yxz@hnu.edu.cn (X. Yuan), huankewanghou024@163.com (H. Wang).

https://doi.org/10.1016/j.apcatb.2017.11.040
Received 5 August 2017; Received in revised form 1 October 2017; Accepted 15 November 2017
Available online 21 November 2017
0926-3373/

embedded with g–C_3N_4 quantum dots were synthesized for methylene blue and methyl orange degradation under the full spectrum [21,28,29]. Especially, the indium sulfide (In_2S_3) has favorable properties of narrow band gap, high stability, low toxicity, and various morphologies including nanoplates, nanotubes, nanorods and hollow microspheres, which makes it can not only as good candidate for broad–spectral photocatalyst, but also as superior sensitizer for wide band gap photocatalysts [30,31]. *Mao* et al. reported that the irregular In_2S_3 nanoparticles with particle size of 5 ~ 20 nm has the relatively high photodegradation abilities under broad–spectral originating from the defective spinel structure [20]. Our groups found that the coupling In_2S_3 with MIL-125(Ti) has synergistic effect on tetracycline degradation over core–shell In_2S_3@MIL-125(Ti) under visible light exposure [32]. However, the limited quantum efficiency as well as the rapid recombination of electrons and holes are still the main drawbacks of In_2S_3.

One of most effective strategy to ameliorate the full–solar–spectrum photocatalytic efficiency of semiconductors is doping with transition metal ions [9,14,33]. It will induce a batho–chromic shift, resulting in the band gap decrease or intra–band gap states formation for more efficient light absorption. Furthermore, the doping can rehibit the recombination of photogenerated electrons and holes, and hence enhancing the photocatalytic efficiency [34]. In recent years, many researchers have devoted their works in doping semiconductor with rare earth ions, as they are able to convert low energy photons (NIR) into higher energy emitted photons (UV or visible light) for excitation of photocatalyst via nonlinear optical effect of upconversion process [25,35,36]. The pioneering investigations of NIR driven photocatalysts based on the upconversion luminescence of rare earth ions was performed by *Qin* et al. who developed a NIR to UV upconversion system comprising TiO_2–coated YF_3:Yb/Tm nanoparticles as the photocatalyst [37]. Afterwards, lanthanide ions with 4f electron configurations doping semiconductor with a new energy level between the valence and conduction band for NIR photocatalysis via upconversion has become the hotspot. To dates, numerous photocatalysts, sunch as Er doped TiO_2 [38], $NaYF_4$:Yb^{3+},Tm@TiO_2 [7], α−$NaYF_4$:Yb,Tm@TiO_2/RGO [39], $NaYF_4$:Yb,Tm/TiO_2/CdS [40,41], $NaYF_4$:Yb,Tm/C_3N_4 [36], Er–Tm–Yb–Bi co–doped $NaY(WO_4)_2$/TiO_2/YF_3 [42], Nd–Er co–doped BiVO4 [43], Er/Yb co–doped Bi_2MoO_6 [33], Yb–Er co–doped $BiVO_4$ [44], Yb–Tm co–doped $BiPO_4$/$BiVO_4$ [45], Yb–Er–Tm co–doped $BiVO_4$ [46], NaGdF4:Er, Yb@$BiFeO_3$ [47], and so on have been designed with fluorescence resonance energy transfer. However, rare attention has been paid on the direct doping of metal sulfides with lanthanides for solar full–spectrum photocatalysis.

In this Article, we have synthesized the Yb and Tm co–doped In_2S_3 through a simple hydrothermal method and evaluated the photocatalytic activity towards chromium (VI) reduction and rhodamine B oxydation under UV−Vis−NIR illumination. The obtained photocatalysts were characterized XRD, SEM, HRTEM, XPS, UV–vis–NIR DRS and so on. The NIR to UV and visible upconversion mechanism has been discussed. Moreover, the possible enhanced photocatalytic mechanism as well as the reusability and stability of the photocatalyst were also investigated.

2. Materials and methods

2.1. Materials

$InCl_3{\cdot}4H_2O$, $YbCl_3{\cdot}4H_2O$, $TmCl_3{\cdot}4H_2O$ and thioacetamide (TAA) were the production of Sinopharm Chemical Regent Co., Ltd (Shanghai, China). All other analytical grade chemicals and the ultrapure water resistivity at 18.25 MΩ.cm were used throughout the experiments.

2.2. Synthesis of Yb^{3+}/Tm^{3+} codoped In_2S_3

To fabricate the Yb^{3+}/Tm^{3+} codoped In_2S_3, 1 mmol of total chlorides including $InCl_3{\cdot}4H_2O$, $YbCl_3{\cdot}4H_2O$ and $TmCl_3{\cdot}4H_2O$ with different mole ratio were dissolved in 30 ml ultrapure water, in which the 1 mmol chlorides. After that, 3 mmol TAA was introduced as a sulfer source. The resultant transparent suspension was sealed in a 100 mL Teflon−lined autoclave and heated in an electric oven at 180 °C for 24 h. After the autoclave cooled down to room temperature, the resulting product was collected by centrifuged and washed successively with deionized water and absolute ethanol several times. Finally, the production was dried in vacuum at 60 °C for 3 h. The samples prepared with different mole ratios of In^{3+}:Yb^{3+}:Tm^{3+} at 189:10:1, 179:20:1, 169:30:1, 159:40:1 and 149:50:1 were denoted as YTIS–1, YTIS–2, YTIS–3, YTIS–4 and YTIS–5, For comparison purposes, conventional In_2S_3 (IS) was synthesized at 1 mmol of $InCl_3{\cdot}4H_2O$ and 3 mmol TAA without the presence of Yb^{3+} and Tm^{3+}. Meanwhile, the Yb^{3+} doped In_2S_3 (YIS) and Tm^{3+} doped In_2S_3 (TIS) were also prepared at optimum proportion, namely, the YIS and TIS were synthesized with 1 mmol total metal ion at mole ratios of In^{3+}:Yb^{3+} of 4:1 and In^{3+}:Tm^{3+} of 199:1, respectively, under the same conditions.

2.3. Characterization methods

The morphologies of samples were observed by using the Environmental scanning electron microscope (SEM, FEI QuANTA 200, USA), and transmission electron micro−scopy (TEM, Tecnai G2 F20, USA). The X–ray diffraction (XRD) patterns were recorded by Bruker AXS D8 Advance diffractometer with Cu–Ka beam source (λ = 1.541 Å). The surface elemental composition analyses were measured based on the X–ray photoelectron spectroscopy (XPS, Thermo Fisher Scientific–K–Alpha 1063, UK) with a resolution of 0.5 eV. The UV−vis−NIR diffuse reflectance spectra (DRS) of the samples were recorded on a UV−vis−NIR spectrophotometer (U−4100, Hitachi, Japan) with an integrating sphere attachment within the range of 200−2600 nm. The up−convertion PL specttra was detected by a Jobin Fluorolog−3−P fluorescent spectrometer coupled with a NIR laser at λ = 980 nm as the excitation source. Photoluminescence(PL) spectroscopy was measured on PerkinElmer LS−55 spectrofluorimeter at room temperature. Photocurrent and Mott–Schottky measurements were performed on a CHI 660D electrochemical workstation (Shanghai Chenhua, China) in 0.5 M Na_2SO_4 electrolyte using a three−electrode cell with the nanostructure materials on FTO as the working electrode, saturated Ag/AgCl and platinum electrode as the counter electrode and the reference electrode, respectively. The electron spin resonance (ESR) signals of radicals $\cdot O_2^-$ spin−trapped by 5, 5-dimethyl-L-pyrroline N-oxide (DMPO) in methanol and h^+ spin−trapped 2,2,6,6-Tetramethylpiperidinooxy (TEMPO) and chlorpromazinehydrochloride (CPH) in aqueous solution with trapping agent of 100 mM were conducted on a Bruker model ESR JES−FA200 spectrometer under NIR light irradiation (λ > 780 nm) at room temperature, the microwave frequency was 9.34 GHz, microwave power was 2 mW, and magnetic field modulation amplitude was 1 G. Three−dimensional excitation−emission matrix fluorescence spectra (3D EMMs) were collected in the excitation wavelengths range of λ_{ex} = 200 ~ 700 nm and in the emission wavelengths range of λ_{em} = 200 ~ 700 nm (F−4500 spectrofluorimeter, Hitachi, Japan).

2.4. Photocatalytic activity

Photocatalytic efficiency of samples for Cr(VI) reduction and RhB decomposition was tested under UV (< 400 nm), visible (400 ~ 760 nm), near–infrared light (> 760 nm) and full−spectra−-light irradiation with a 300 W Xenon lamp (CEL−HXF300, Beijing CEL Tech. Co., Ltd.) at 14 V and 21 A that equipped with a cooling system for temperature control. Typically, 30 mg of photocatalysts was magnetically stirred in 100 mL of C_0 10 mg L^{-1} Cr(VI) or 40 mg L^{-1} RhB solution in the dark for 60 min to reach the adsorption–desorption quilibrium. During the light illumination, little samples were draw out

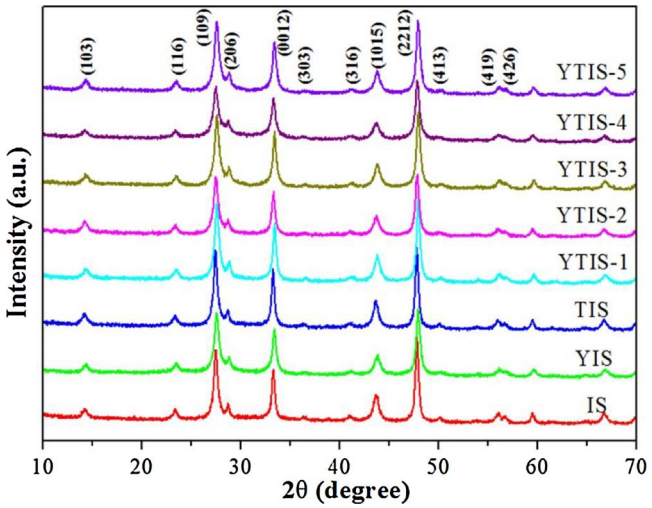

Fig. 1. The XRD pattern of samples.

and filtrated by 0.22 m PTFE syringefilters for Cr(VI) and RhB concentration detection with a UV–vis spectrophotometer (UV－2250, SHI－MADZU Corporation, Japan). The photocatalyst of YTIS–5 after photocatalysis was filtrated and washed with water for three times to remove residual impurities, and then dried at 60 °C for recycling.

3. Results and discussions

3.1. Characterization

The crystal structure of the obtained samples were examined by XRD. As shown in Fig. 1, all of the diffraction peaks of samples match well with the JCPDS card file No. 25–0390, indicating tetragonal crystalline phase of In_2S_3. Specifically, the peaks located at 2θ = 14.2°, 23.3°, 27.4°, 28.7°, 33.3°, 36.3°, 40.9°, 43.7°, 47.8°, 50.2°, 56.1° and 56.7° are distinctly indexed to the (103), (116), (109), (206), (0012), (303), (316), (1015), (2212), (413), (419) and (426) crystal planes, respectively. Moreover, the Yb^{3+}/Tm^{3+} doping do not change the phase structure, and no other phases such as Yb_2S_3 and Tm_2S_3 have been detected, which suggests that the as–prepared Yb^{3+}/Tm^{3+} co–-doped In_2S_3 samples are well–crystallized.

The morphology characteristics observed by SEM are shown in Fig. 2(a–i). The pure In_2S_3 sample (Fig. 2a and b) presents the ball–like structure with uneven size, which consists of numerous bending 2D nanosheets that are mutually interwoven and self－assembled into 3D hierarchical network forming the flower－like microsphere with

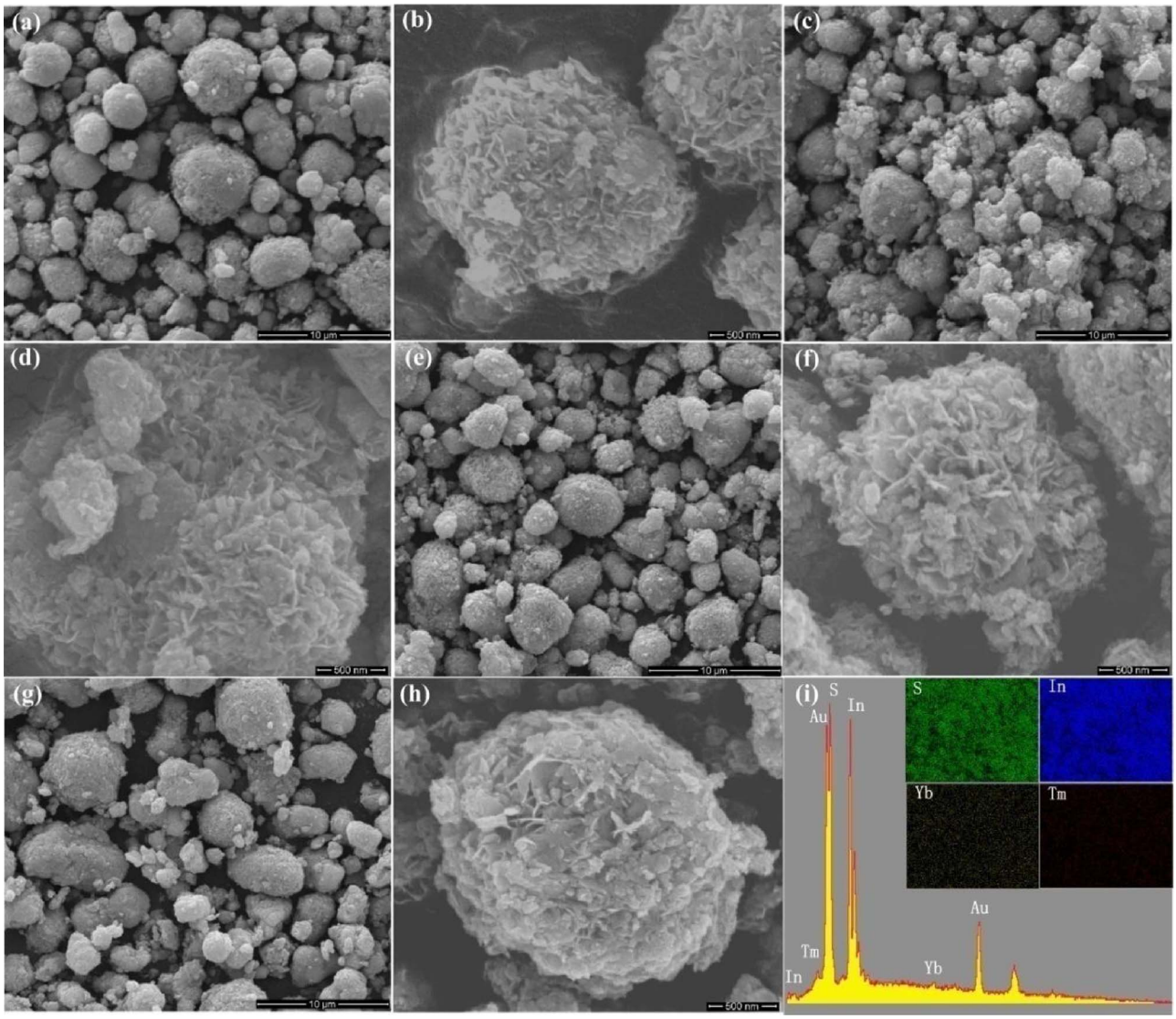

Fig. 2. The SEM images of IS (a and b), YIS (c and d), TIS (e and f) and YTIS-4 (g and h); The EDS spectra (i) of YTIS-4 and element mapping.

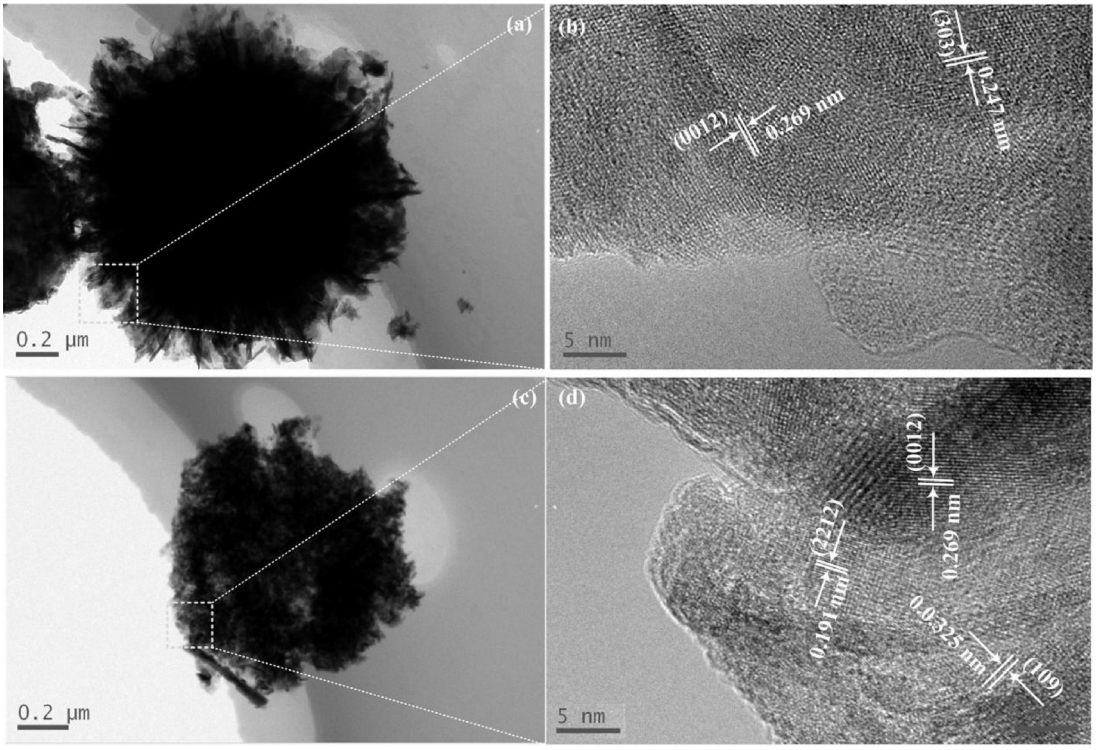

Fig. 3. The TEM and HRTEM images of IS (a and b) and YTIS-4 (c and d).

numerous pores. Fig. 2c–h present the SEM images and the corresponding higher magnification structure of YIS, TIS and YTIS–4, respectively. It can be seen that there are some irregular particles unevenly distributed over the surface of lanthanides doped samples. This may involve the three–stage morphological evolution process, namely, the pre–crystallized nuclei and crystal growth, oriented attachment of prisms, and inside–out Ostwald ripening of flowery hierarchies. During the reaction, the precursor decomposed and the In^{3+} with S^{2-} ions quickly pre–crystallized nuclei and crystal growth into prisms. Subsequently, the prisms are further oriented together to form the 2D nanosheets originating from the anisotropic structure of crystal. As the surfaces of the nanosheets are in contact with the surrounding solution, the interior flowery hierarchies had a tendency to collapse, and result in some rupture parts on the surface [34,48]. The energy dispersive spectrum (EDS) of YTIS–4 (Fig. 2i) shows that the YTIS–4 sample consists of uniformly distributed elements of In, Yb, Tm and S elements.

Fig. 3 comparatively exhibits the TEM image of In_2S_3 and YTIS–4. From Fig. 3a and c, it can be found that the pure In_2S_3 has a more dense spherical structure than YTIS–4, which matches well with SEM result that YTIS–4 has some irregular particles on the surface. As shown in Fig. 3b, two different lattice fringes ascribing to the (303) and (0012) crystallographic planes with the d–spacing of 0.247 nm and 0.269 nm, respectively, are found in the HRTEM image of pure In_2S_3. In contrast, more crystal faces can be observed from HRTEM image of YTIS–4. The interplanar spacings of 0.191 nm, 0.269 nm and 0.325 nm attribute to the planes (2212), (0012) and (109), respectively, which are onsistent with the crystallographic plane of tetragonal In_2S_3.

The surface chemical composition and electronic environment of the as–prepared YTIS–4 was analysized by XPS. As shown in Fig. 4a, the full–scan spectrum reveals that the elements In, Yb, Tm and S exist in the YTIS–4. The high–resolution spectra of S 2p, In 3d, Yb 3d and Tm 3d are presented in Fig. 4b–e, respectively. The peak of S2p (Fig. 4b) can be deconvoluted into two symmetric Gaussian curves at 161.6 eV and 162.8 eV, corresponding to the S $2p_{3/2}$ and S $2p_{1/2}$ transitions, respectively. As shown in Fig. 4c, the spectra of In 3d exhibits two symmetrical peaks at the binding energy of 445.0 eV and 452.6 eV assigning to the In $3d_{5/2}$ and In $3d_{3/2}$, respectively. The spin–orbit splitting difference of S 2p and In 3d are calculated to be 7.6 eV and 1.1 eV, which suggests that the S and In element exists in the valence state of S^{2-} and In^{3+} in YTIS–4, respectively [20,32]. The XPS signals of Yb 3d (Fig. 4d) and Tm 3d (Fig. 4e) were observed at binding energies of 186.2 eV and 178.5 eV, which is in agreement with the previous reports [46], indicating the successful incorporation of Yb^{3+} and Tm^{3+} into In_2S_3 crystal.

Due to that the optical absorption property is one of the most important factor in determining the photocatalytic performance of semiconductor, the UV–vis–NIR DRS of all samples are conducted and shown in Fig. 5a. It can be seen that the pure IS shows significant absorption in both UV and visible light region, which facilitates adsorption of the photon energy that is generated from the upconversion process of Yb^{3+}/Tm^{3+} in YTIS. In addition, the IS displays two absorption peaks at 1440 nm and 1942 nm due to the defective valence band of IS, which is consistent with the previous report by *Gao* et al. [20]. As the IS doped with Yb^{3+}/Tm^{3+}, the adsorption intensity in the region of 200–2600 nm is remarkably enhanced, which implies the possibility of expected photocatalytic performance for Yb^{3+}/Tm^{3+} codoped IS under ultraviolet to near–infrared light irradiation. Moreover, it is worth noting that the YIS and YTIS samples shows the new broad absorption peaks between 910 nm and 1010 nm compared with IS and TIS, which is ascribed to the $^2F_{7/2} \rightarrow {}^2F^{5/2}$ transition of Yb^{3+} ions [7,47]. Among the samples of YTIS, the YTIS − 4 shows the strongest absorption between 200–2600 nm. The band gap (Eg) energy of all samples are calculated by the formula $Eg = 1240/\lambda$ (λ is the absorption edge wavelength). It is found that DRS spectrums of the Yb^{3+}/Tm^{3+} doped In_2S_3 display the steeper edges than pure In_2S_3 in the profile, which may be attributed to the optical transition of the intermediate energy states within energy gap of IS [44]. The calculated Eg of IS, YTIS, TIS and YTIS − 1 to YTIS − 4 is 1.77 eV, 1.78 eV, 1.85 eV, 1.78 eV, 1.79 eV, 1.79 eV, 1.80 eV and 1.79 eV, respectively. To better understand the flat band potentials (V_{fb}) change related to electronic properties between IS and YTIS, Mott–Sckottky (MS) measurement was carried out in darkness by using the impedance technique. Fig. 5b

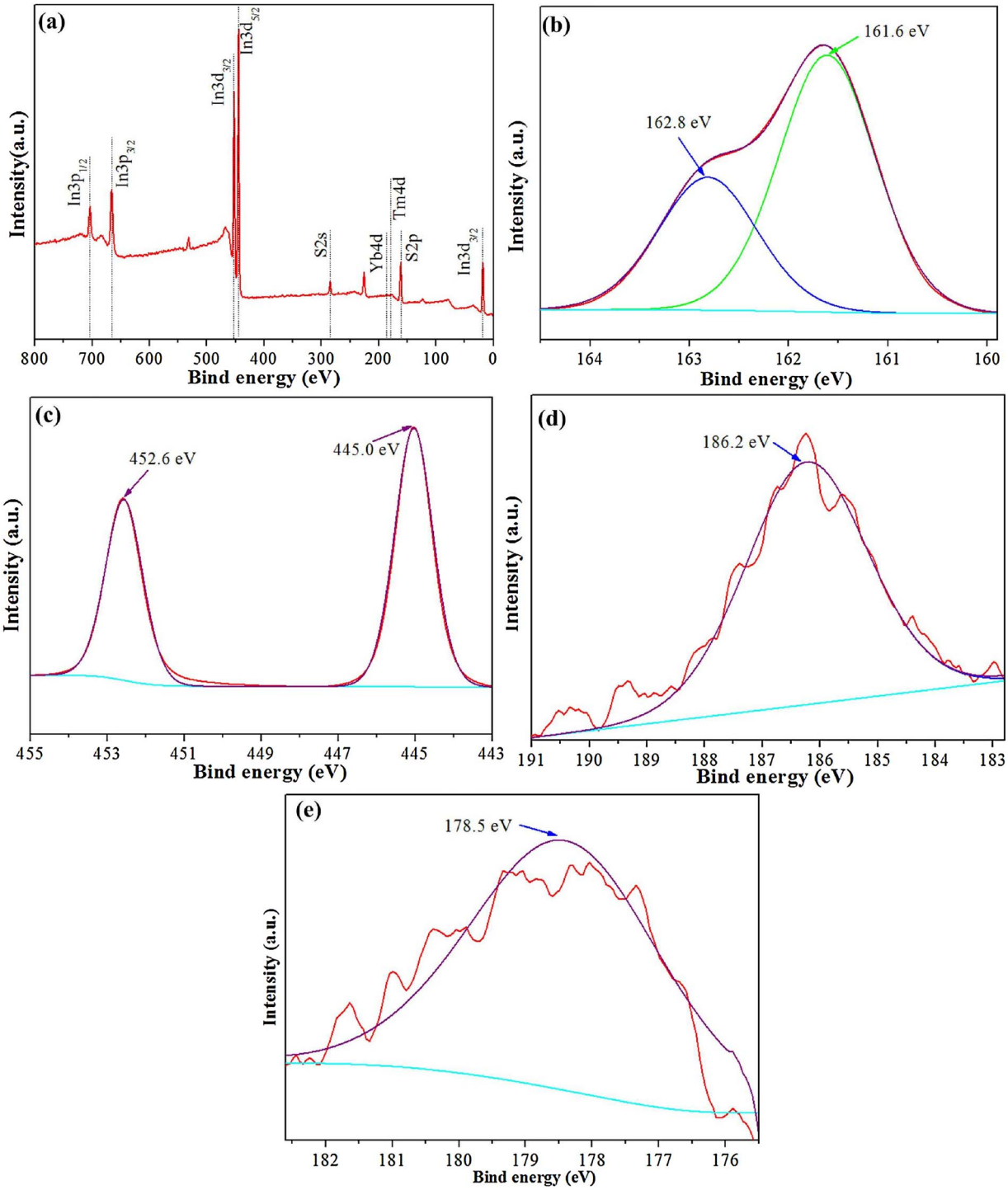

Fig. 4. The XPS spectra of YTIS-4 sample: (a) survey spectrum, (b) S2p, (c) In3d, (d) Yb3d and (e) Tm3d;.

presents the Mott–Schottky plot as $1/C^2$ vs. *potential (V vs Ag/AgCl)*. It can be observed that the Mott–Schottky curves of IS and YTIS are reversed sigmoidal plots with an overall shape consistent with the typical for n-type semiconductors [49]. The V_{fb}, as calculated from the x − axis intercepts of the linear region, were found to be −0.48 and −0.51 V vs. Ag/AgCl, corresponding to ca. −0.28 V and −0.31 V vs NHE for IS and YTIS-4, respectively. It is well known that the conduction band potential (E_{CB}) of n-type semiconductor is more negative (0–0.2 V) than the V_{fb}, which depends on the electron effective mass and the carrier concentration [50]. Here, the voltage difference between the E_{CB} and the V_{fb} is set to 0.1 V. Thus, the negative shift in Fermi level of YTIS causes the E_{CB} shift of YTIS − 4 from −0.38 V to −0.41 V vs NHE, which could facililate the oxygen reduction reaction with a stronger reductive power. Combined with the Eg estimated from UV − vis − NIR DRS spectra, the valence bands (VB) of IS and YTIS − 4 are calculated to be +1.39 V vs NHE according to the equations of $E_{CB} = E_{VB} - Eg$. These data clearly demonstrate the changes in electronic structures of In_2S_3 after Yb^{3+}/Tm^{3+} doping, which may be attributed to the slight changes of lattice structure, such as the formation of intermediate energy states and/or more sulfur vacancies. Such variations in the electronic structures may alter the delocalization degree of photogenerated carriers, and futher result in which different separation and migration rate of

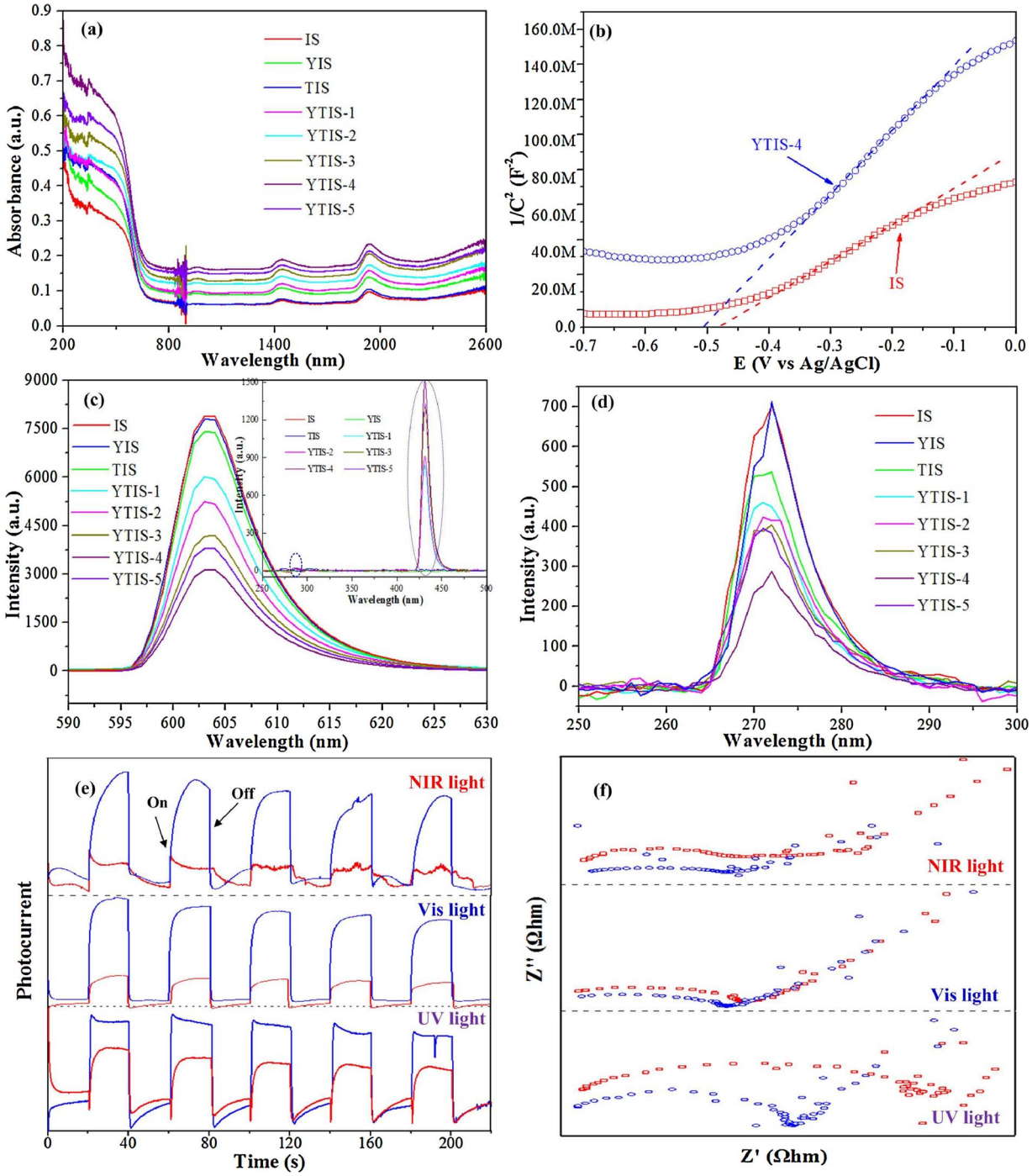

Fig. 5. (a) The UV–vis-NIR DRS spectrum of samples; (b) Mott-Schottky (MS) plots of In_2S_3 and YTIS-4 electrodes; (c) The photoluminescence spectra of samples under excitiation of 600 nm (inset is corresponding emission spectra in range of 250 nm ~500 nm); (d) The photoluminescence spectra of samples under excitiation of 270 nm; (e) The I-T curves and (f) the EIS responses of YTIS-4 (blue curve) and In_2S_3 (red curve) under NIR, visible light and UV irridiation. (For interpretation of the references to colour in this figure legend, the reader is referred to the web version of this article.)

electron and hole [51].

The photoluminescence (PL) spectra at the excitation wavelength of 600 nm and 270 nm are conducted to evaluate the separation capacity of the photoinduced carriers. As shown in Fig. 5c, the PL spectrums of pure IS show the strong emission at ~ 600 nm. With the doping of Yb^{3+}/Tm^{3+}, the PL intensity significantly decreases, and the YTIS − 4 presents the lowest, which indicates that Yb^{3+}/Tm^{3+} doping can retard the recombination of photogenerated electron–hole pairs and promote the separation of electron–hole. Moreover, as can be seen from the inset in Fig. 5c, under the excitation wavelength of 600 nm, the Yb^{3+}/Tm^{3+} codoped In_2S_3 samples show the intense emission peak in range of 420 ~ 460 nm and weakly broad emission peak at 282 ~ 294 nm, which corresponds to the $^1I_6 \rightarrow {}^3F_4$ and $^1G_4 \rightarrow {}^3H_6$ transitions of Tm^{3+} ions, respectively, indicating the upconversion effect of Yb^{3+}/Tm^{3+} codoped In_2S_3 [7,37]. Fig. 5d depicts the PL spectrums of IS and YTIS samples at the UV light excitation of 270 nm. It is also found that as Yb^{3+}/Tm^{3+} doping in In_2S_3, the PL intensity at ~270 nm decreases obviously, which is consistent with the results under visible light excitation, confirming the improvement of charge separation efficiency. As the lanthanides incorporated in the lattice sites, an intermediate

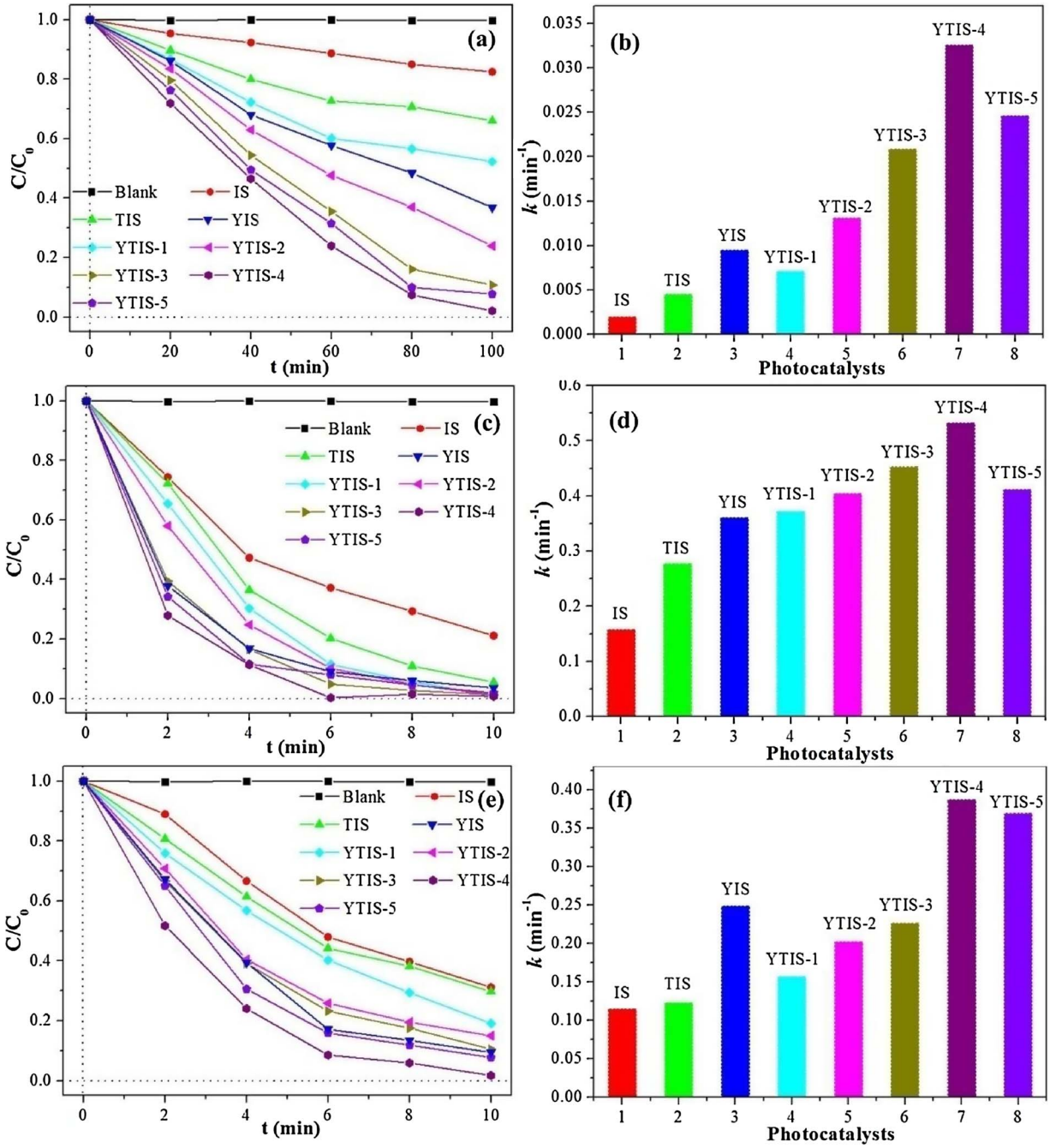

Fig. 6. The photocatalytic reduction performance of Cr(VI) by photocatalysts under NIR (a), Vis (c) and UV (e) irradiation; The first–order–kinetics of Cr(VI) reduction over photocatalysts under NIR (b), Vis (d) and UV (f) irradiation.

energy states may form below the CB of the photocatalyst, which can improve the optical absorption and electron – hole separation due to its role of electron trapping centers and interfacial charge transfer mediator [43,44,51].

To further testify the separation efficiency of photogenerated electron – holes pairs, the transient photocurrent value of IS and YTIS – 4 electrodes are recorded for several on–off cycles of various illumination with 20 s intervals in 0.5 M Na_2SO_4 solution. It can be seen from Fig. 5e that the transient photocurrent responses of samples at light – on and – off are stable. The photocurrent response of YTIS – 4 is greatly enhanced compared to the pure IS at the NIR, vis and UV light irradiation, which reveals that the Yb^{3+}/Tm^{3+} doping can significantly improve the separation efficency of photo – generated electron – hole pairs, and thus contribute to enhancing the photocatalytic performance. The electrochemical impedance spectroscopy (EIS) is an effective electrochemical method to explain the electron – transfer efficiency at the electrodes by comparing the arc radius of Nyquist plots. Generally, the smaller arc radius means the lower charge transfer resistance at the semiconductor/electrolyte interface. As shown in Fig. 5f, the Nyquist arc radius of YTIS – 4 are smaller than that of IS under UV, visible and NIR light exposure, which futher indicates the lower electric resistance and higher photo – generated charge separation rate. Therefore, the YTIS may be a promising material for photocatalytic application.

3.2. Photocatalytic activity

In order to prove the photocatalytic activity of the Yb^{3+}/Tm^{3+} doped In_2S_3, the photoreduction of Cr (VI) and photodegradation of

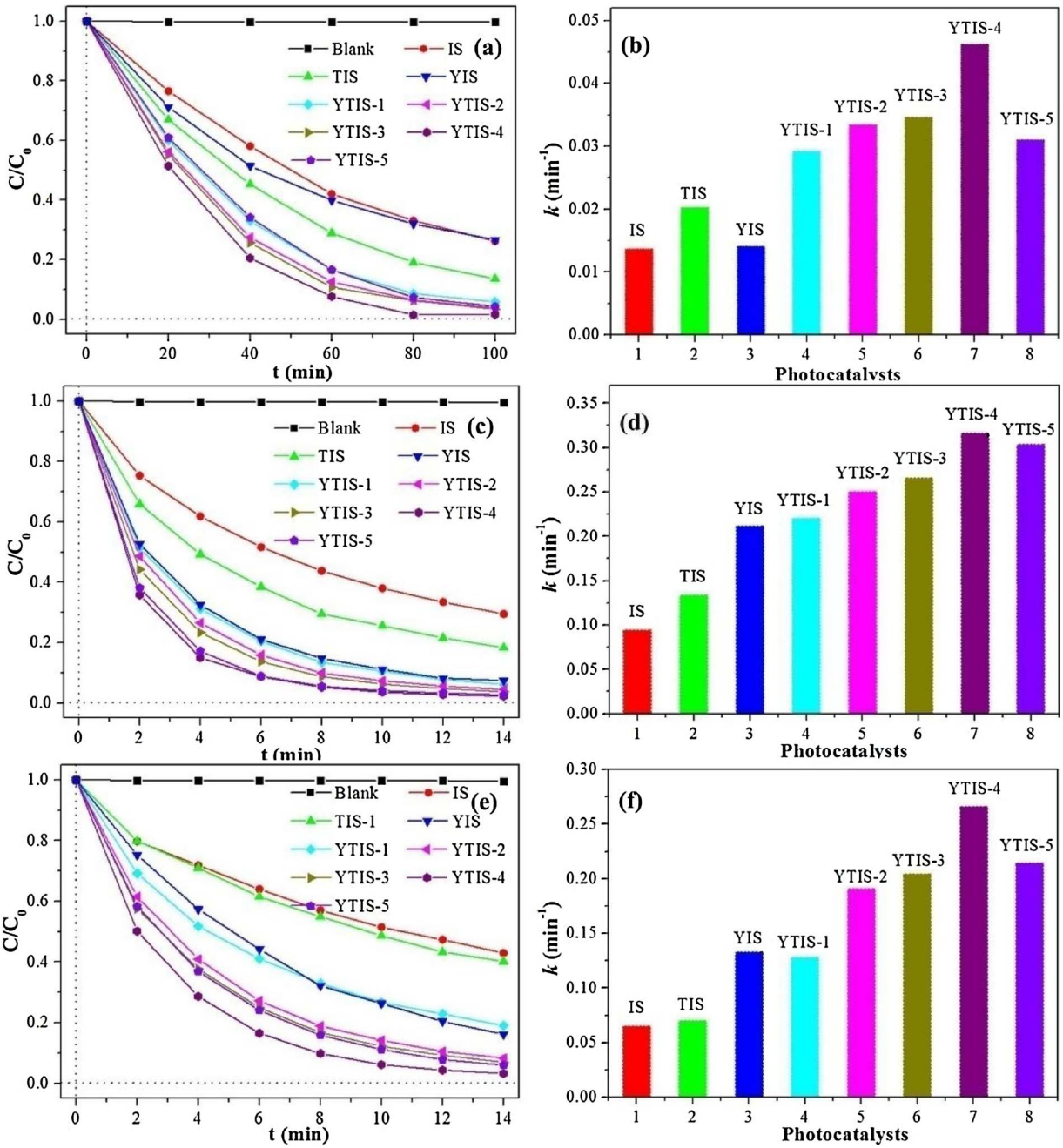

Fig. 7. The photocatalytic degradation performance of RhB by photocatalysts under NIR (a), Vis (c) and UV (e) irradiation. The first–order–kinetics of RhB degradation over photocatalysts under NIR (b), Vis (d) and UV (f) irradiation.

rhodamine B in aqueous solution under UV, vis, NIR, and full-spectrum-light are implemented. Figs. 6 and 7 present the photocatalytic performance of all samples for Cr (VI) reduction and rhodamine B oxidation, respectively. It can be found that the photocatalytic performance is significantly enhanced in the presence of YTIS compared with IS under the three kinds of light source irradiation, and the YTIS − 4 shows the optimum photocatalytic performance. Under NIR illumination for 100 min, the Cr(VI) reduction (Fig. 6a) and RhB degradation (Fig. 7a) efficiency of IS is 18.5% and 73.8%, resepctively, which could be ascribed to the NIR adsorption at 1440 nm and 1942 nm of pure IS depending on the presence of sulfur vacancies or oxygen in the In_2S_3 nanoparticle surface. *Mao* et al. considered that the sulfur vacancies and oxygen contribute to the formation of defect spinal structure, which induces the generation of electron–hole pairs under the irradiation of NIR light [20]. Comparatively, the YTIS − 4 has the more preferable photocatalytic ability towards Cr(VI) reduction and RhB degradation of 97.9% and 98.4%, respectively, after 100 min of NIR irradiation. The enhancement of photocatalytic efficiency under NIR irradiation may rely on the improved NIR adsorption and the upconversion of low energy photon to UV and visible light for extation of In_2S_3 by Yb^{3+}/Tm^{3+} [37]. As despicted in Figs. 6 (c,e) and 7 (c,e), the Cr(VI) reduction and RhB degradation are the fast process under vis and UV irradition, which testifies that YTIS could be an effective photocatalyst. For Cr(VI) reduction, the photocatalytic efficiency of YTIS − 4 is 99.3% and 98.3% by vis and UV light illumination for 10 min, respectively, which is much higher than the corresponding value of 78.9% and 68.8% in presence of IS. Similarly, after irradiation of vis and UV for 14 min, the RhB removal efficiency of YTIS − 4 is 97.3% and 96.8%, respectively, while that of IS is 70.5% and 57.1%, respectively, which is due to the effcient interfacial charge transfer and electron − hole pair separation by

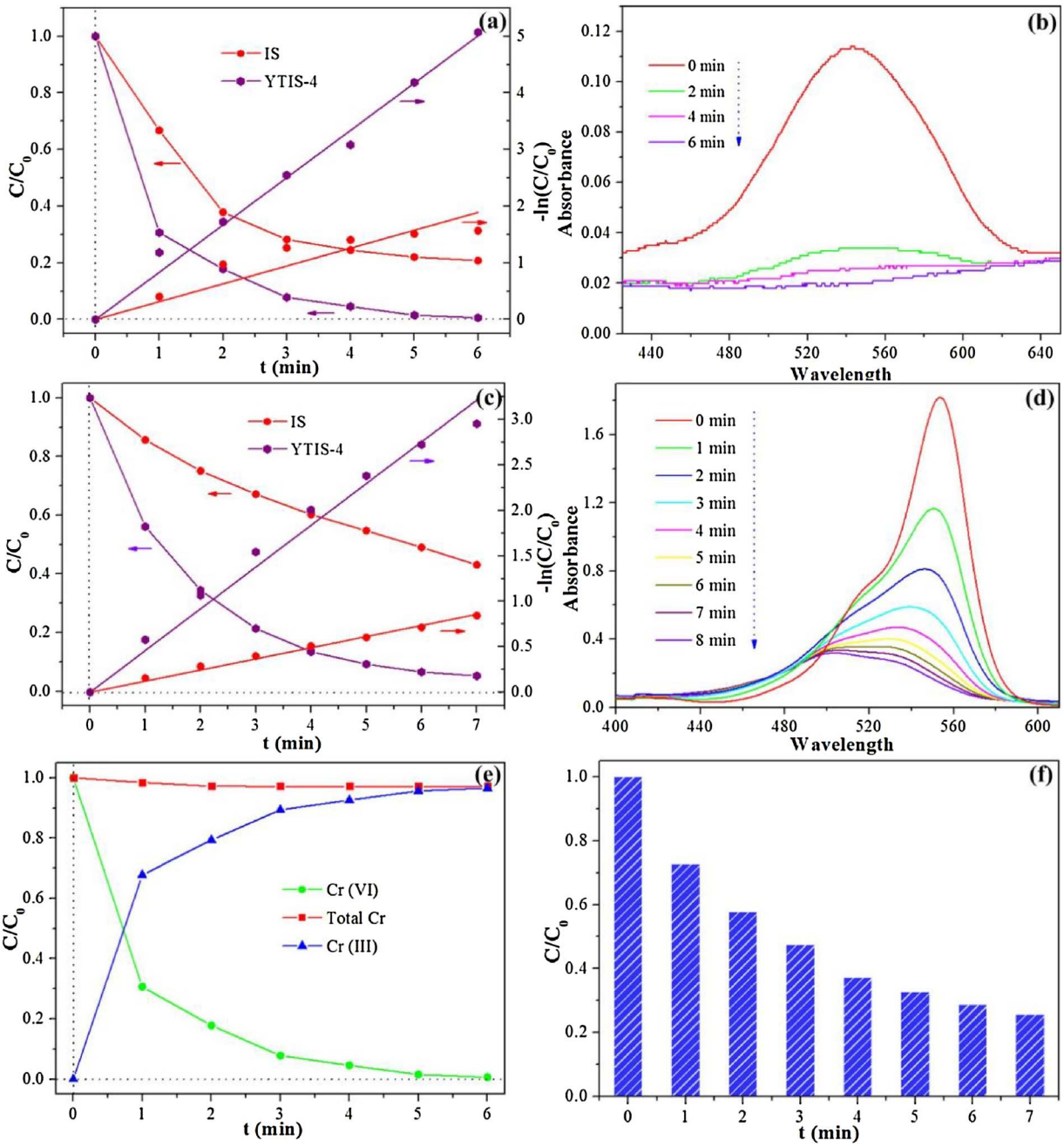

Fig. 8. The photocatalytic performance under full spectra light irradiation: Cr(VI) reduction (a) and RhB degradation (c), changes in the UV–vis absorption spectra of Cr(VI)– diphenylcarbazide complex (b) and RhB (d) over the YTIS–4, the change in total Cr, Cr(VI) and Cr(III) (e), and the change in TOC during RhB degradation.

intermediate energy states in YTIS [46].

To gain insight into the reaction kinetics of Cr(VI) reduction and RhB degradation under differnt light saurces, the experimental data are fitted with the Langmuir–Hinshelwood (L–H) first–order kinetic model of $-ln(C/C_0) = k_1 t$, where C_0 and C (mg/L) is the initial concentration and residual concentration at time t (min), respectively [28,52,53]. The k_1 (min^{-1}) is the apparent rate constant, and the k_1 values of different samples are shown in Figs. 6 and 7. It can be found that the Yb^{3+} individually doped IS and Yb^{3+}/Tm^{3+} codoped IS display the significant higher photocatalytic activities towards Cr(VI) and RhB removal than the pure IS, revealing the noticeable effect of Yb^{3+} – doped In_2S_3 on the degradation process. With the increasing of ratio of doped Yb^{3+}/Tm^{3+}, the rate constants of YTIS exhibit the tendency to increase first and then down, and the YTIS – 4 has the highest rate constant, which is consistent with the light decay of the reaction rates with higher Yb^{3+} loadings reported by *Obregon* et al. [44]. The rate constant value of YTIS – 4 for Cr(VI) reduction is 0.033 min^{-1}, 0.533 min^{-1} and 0.387 min^{-1}, which is 16.67, 3.36 and 3.36 times than that of IS driven by NIR, vis and UV light, respectively. Similarly, the RhB degradation rate constant of YTIS – 4 under NIR (0.046 min^{-1}), vis (0.317 min^{-1}) and UV (0.266 min^{-1}) irradiation is 3.38, 3.35 and 4.10 times than that of IS, respectively. Moreover, to quantitatively comprehend the effect of Yb^{3+} and Tm^{3+} co – doping on the photocatalytic activity, the synergy index (SI) is estimated as the definition of $SI = k_{1(YTIS-4)}/(k_{1(YIS)} + k_{1(TIS)})$ [54]. According to the datas presented in Figs. 6 and 7, the value of SI is 2.32, 0.83 and 1.04 for Cr(VI) reduction, 1.35, 0.92 and 1.31 for RhB degradation by illumination of NIR, vis and UV light, which indicates that the Yb^{3+} and Tm^{3+} co – doping has the kinetic synergic effect under NIR and UV irradiation.

To further demonstrate the excellent photocatalytic performance of

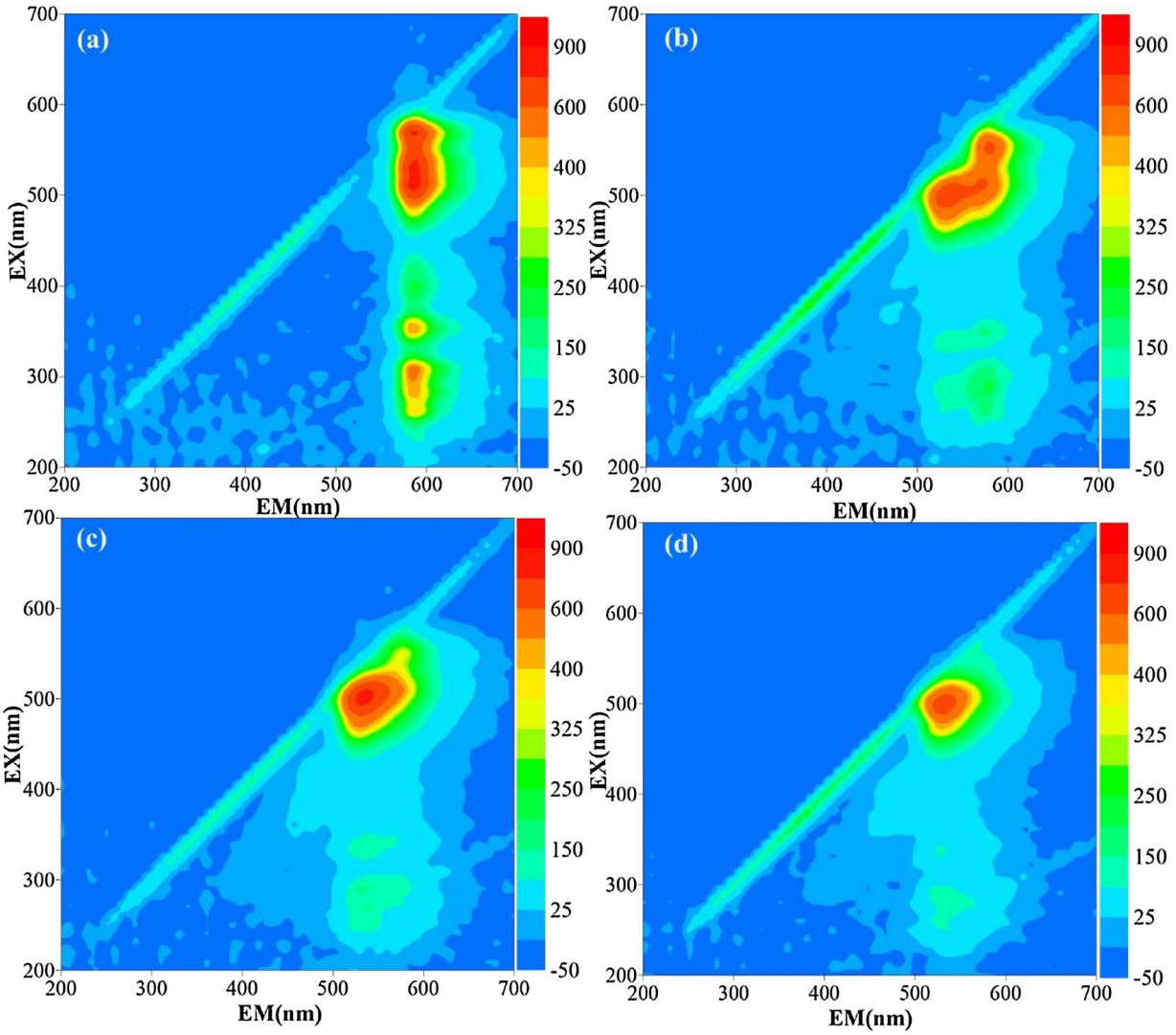

Fig. 9. The time-dependent 3D EEMs of RhB under full spectra light irradiation catalysized by YTIS-4 : (a) 0 min, (b) 2 min, (c) 4 min and (d) 6 min.

YTIS − 4, the photoreduction of Cr(VI) and degradation of RhB are conducted under the full-spectrum-illumination. As shown in Fig. 8a and c, the Cr (VI) and RhB removal efficiency of YTIS − 4 is 99.4% and 94.8% for irradiation 6 min and 7 min, respectively, indicating that the YTIS − 4 is a fast and efficient photocatalyst. In contrast to this, the corresponding photocatalytic performance of pure In_2S_3 is only 79.2% and 56.9% for Cr(VI) and RhB isolation. The UV–vis absorption spectrums of Cr(VI)–diphenylcarbazide complex and RhB as a function of the irradiation time are illustrated in Fig. 8b and d, respectively. It can be seen that the absorption intensity of Cr(VI)–diphenylcarbazide complex at 545 nm decreases dramatically to flat eventually with the increase of irradiation time from 0 to 6 min, indicating that the Cr (VI) is almost completely reduced by YTIS − 4. As for RhB, it shows the similar trend with regards to absorption peak at 554 nm, meanwhile, the obvious blue shift appears in the adsorbance curve, which is attributed to the consecutive deethylation process of RhB during the degradation [43]. The fitting lines of Langmuir–Hinshelwood (L–H) first–order to experiment data are presented in Fig. 8a and c. The rate constant value of YTIS − 4 for Cr (VI) reduction and RhB degradation is 0.683 min^{-1} and 0.459 min^{-1}, which is 2.17 and 5.60 times than that of pure In_2S_3 for Cr (VI) reduction and RhB degradation, respectively. The species of Cr ions residual in the supernatant after photocatalysis in presence of YTIS − 4 are measured by inductively coupled plasma (ICP) emission spectrometer, and the results are shown in Fig. 8e. The total Cr is almost maintained at the same level, which is ascribed to the dynamic equilibrium of adsorption − desorption of total Cr during the illumination process although the valence of Cr changes. As the content decreases of Cr(VI), the concentration of Cr(III) increases accordingly, implying the successful reduction of Cr(VI) to Cr(III). In addition, the total organic carbon (TOC) is performed to determine the mineralization of RhB. As depicted in Fig. 8f, the TOC removal rate of RhB solution is 74.4% after 7 min irradiation, indicating the favorable mineralization properties of YTIS − 4. Further information of change in property of RhB solution during full-spectra-light irradiation is recorded by the three − dimensional excitation − emission matrix fluorescence spectra (3D EMMs). It can be seen from Fig. 9a, the pure RhB shows several peaks at EX/EM of 305/585, 355/585, 515/585 and 570/585 nm in EEM spectra, which is attributed to chromophore, e.g. phenylamino, carbonyl exited in RhB. As the photocatalytic reaction processed (Fig. 9b and c), the above-mentioned peaks gradually disappears and a new peak appeared at EX/EM of 505.0/535.0 nm, which may ascribed to the N − deethylated intermediates. Moreover, the fluorescence intensity (Fig. 9d) of 505.0/535.0 nm significantly decreases after 6 min full-spectra-light irradiation, indicating that the intermediates are gradually decomposited into smaller, undetectable molecules by YTIS − 4.

Although the considerable photoactivities of the YTIS samples have been verified, their stability for reutilization in terms of practical application is unknown. To measure the recyclability of the Yb^{3+}/Tm^{3+}

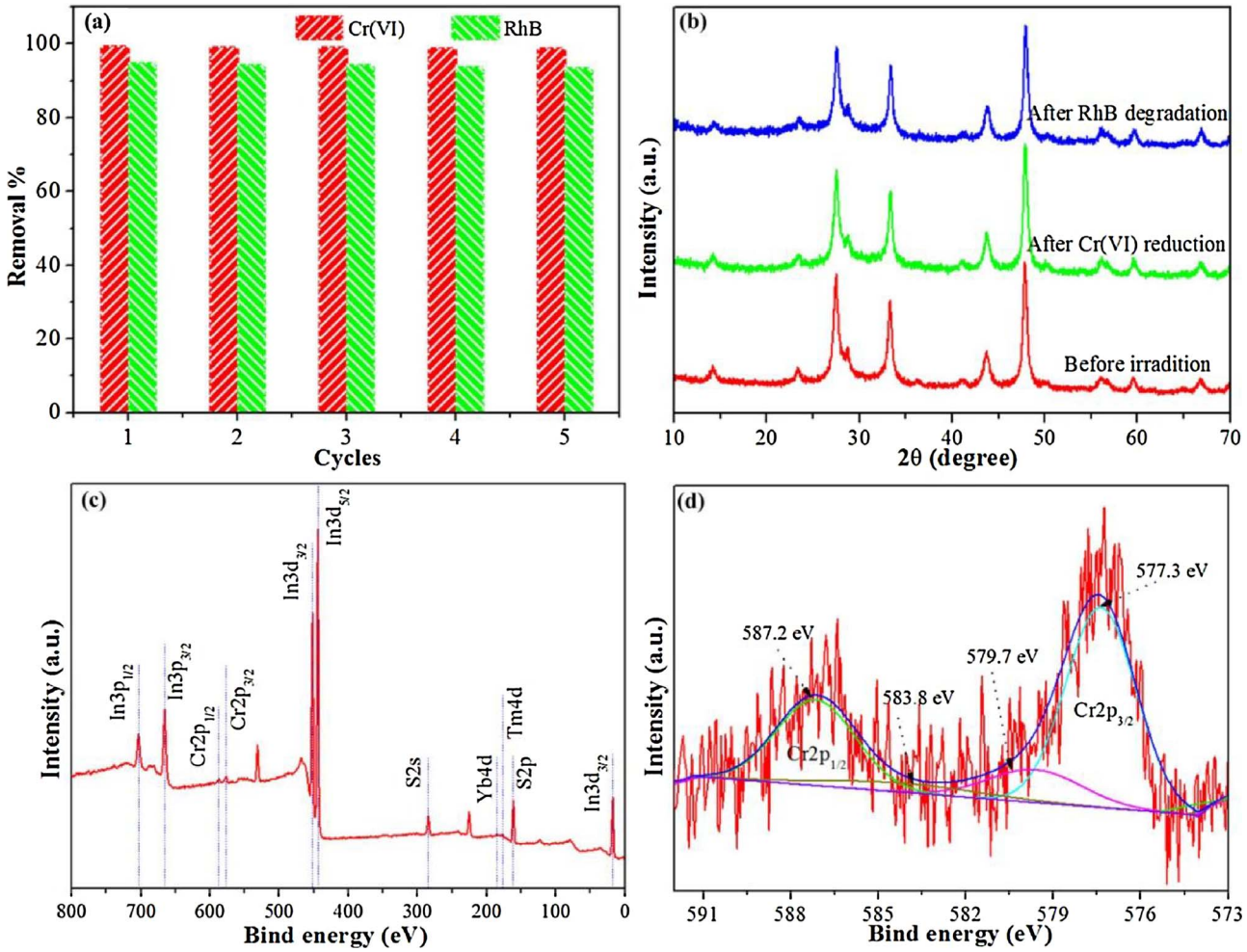

Fig. 10. The repeated photocatalytic experiments of YTIS-4 for Cr (VI) reduction and RhB degradation under full spectra light irradiation (a), and the XRD pattern of the YTIS–4 after 5th photocatalytic cycle (b); The XPS survey spectrum of YTIS–4 after Cr(VI) photoreduction (c) and the high–resolution spectra of Cr2p (d) under full spectra light irradiation;.

codoped In_2S_3, the YTIS − 4 sample is collected after the photocatalytic reaction under full-spectra-light illumination. As presented in Fig. 10a, the photocatalytic activity of YTIS − 4 sample has no apparent deactivation even after five successive recycles, in which the photocatalytic efficiency with regard to Cr (VI) reduction and RhB degradation still remains at 98.6% and 94.1%, respectively. The XRD patterns of YTIS − 4 before and after 5th run cycle are shown in Fig. 10b. It can be observed that the diffraction peaks of recycled YTIS − 4 are almost consistent with that of fresh YTIS − 4, indicating that no obvious change in the phase and structure of recycled YTIS − 4. This can be futher confirmed by the chemical constituent of recycled YTIS − 4 after Cr (VI) reduction analyzed by XPS. The full–scan spectrum (Fig. 10c) also presents a very similar result to the fresh YTIS − 4 (Fig. 4a), except for two new peaks assigning to Cr 2p. As depicted in Fig. 10d, the high resolution spectra of Cr 2p peaks can be curve − fitted with numerous peaks. The peak components at around 583.8 eV and 587.2 eV belong to Cr (VI) origining from Cr $2p_{1/2}$ orbitals. The other two peaks at 577.3 eV and 579.7 eV are related to the characteristic binding energies of the Cr $2p_{3/2}$ orbitals assigning to Cr(III) [5,55]. The appearance of Cr (III) further confirms the reduction of Cr(VI) under full-spectra-light irradiation.

3.3. Photocatalytic mechanism

To undstand the intrinsic photocatalytic mechanism of Cr (VI) reduction and RhB degradation in depth, the main reactive species during the reaction process are inveatigated by the trapping experiment over the YTIS − 4 sample. The triethanolamine, p − benzoquinone and isopropanol are selected for RhB degradation as the scavengers of hole (h^+), superoxide radical ($\cdot O_2^-$) and hydroxyl radical ($\cdot$OH), respectively, while the ethanol and EDTA − 2Na are used as the h^+ scavenger, and the $KBrO_3$ is choosed as electronic capture agent for Cr (VI) removal. As presented in Fig. 11a, the RhB photodegradation efficiency of YTIS − 4 decreases dramatically from 98.4% to 10.1% and 14.7% with the addition of triethanolamine and p − benzoquinone, implying that the h^+ and $\cdot O_2^-$ are the main oxidative species in attacking RhB molecule under NIR irradiation. On the contrary, the presence of isopropanol has no obvious impact on RhB removal, demonstrating that the $\cdot$OH might not be the predominant active species. For Cr (VI) reduction (Fig. 11b), the introduction of $KBrO_3$ results in a significant declination of the Cr(VI) reduction rate from 97.9% to 14.5%, while the addition of ethanol and EDTA − 2Na improved the Cr(VI) reduction efficiency greatly due to that the ethanol and EDTA − 2Na can capture the photo − induced holes promoting the separation of electron − hole pairs.

To confirm the generation of reactive oxygen species under NIR irradiation, the electron spin resonance (ESR) spin − trap experiment was performed with DMPO and TEMPO − CPH. It can be found from Fig. 11c that four signals assigned to DMPO − $\cdot O_2^-$ generate and are enhanced with extension of NIR illumination time from 5 to 10 min, confirming the formation of the $\cdot O_2^-$ radicals over YTIS − 4 for RhB degradation [1]. In darkness, the signal of spin − trapped TEMPO − CPH − h^+ is observed, which is attributing to sulfur vacancies resulted from lattice defects. Such vacancies have the favorable electron

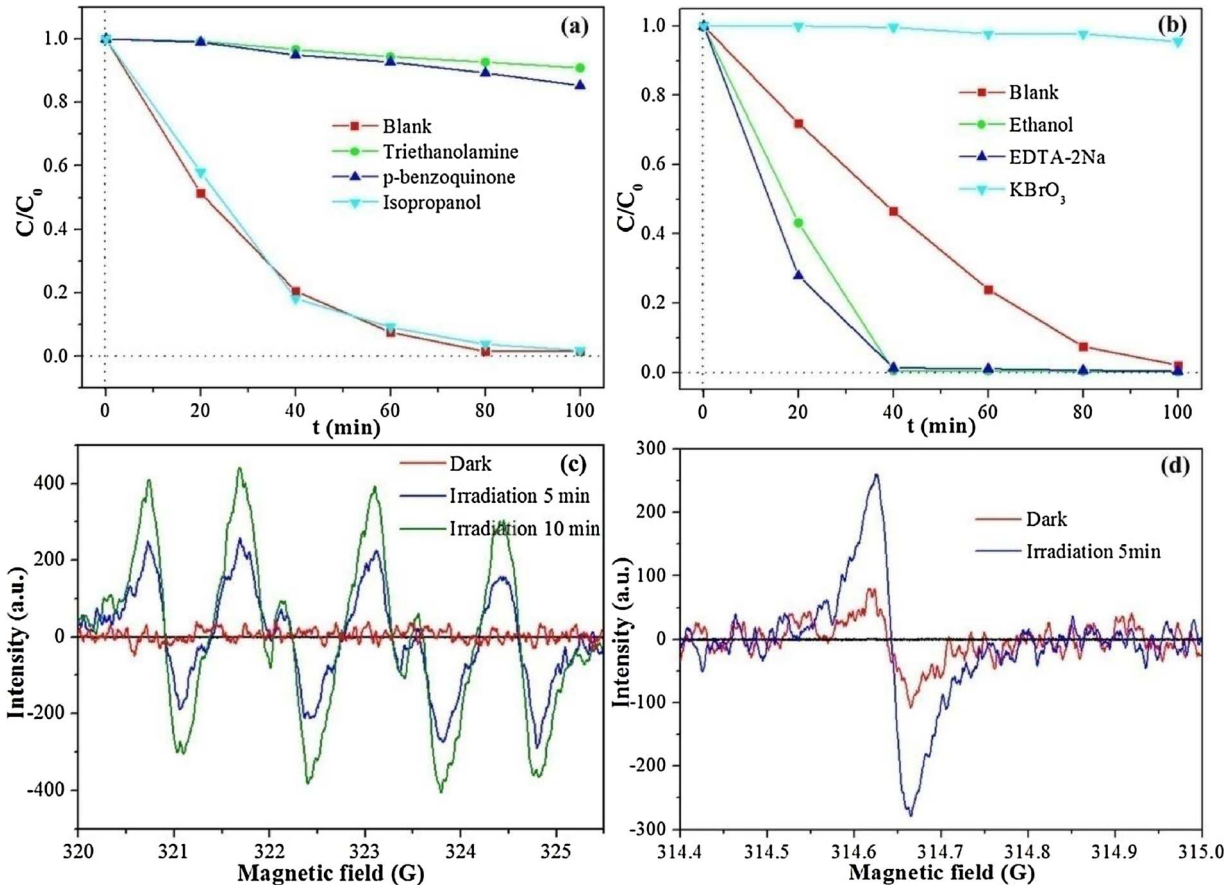

Fig. 11. Trapping experiment of the active species for the degradation of RhB (a) and reduction of Cr (VI) (b) under NIR irradiation; ESR spectra of DMPO spin – trapping for $\cdot O^{2-}$ (c), TEMPO – CPH spin – trapping h^+ (d) under NIR irradiation.

affinity to serve as electron traps, which facilitates the efficient separation of charge carriers [56]. When exposed the YTIS to NIR light for 5 min, the signal increases obviously, indicating that the h^+ could be the contributor for the decompotion of RhB, and also demonstrating the generation of electrons for Cr (VI) reduction from the side.

Upon the illumination of NIR, Yb^{3+} and Tm^{3+} doped in In_2S_3 can adsorbed the light photons and then convert them into higher energy emitted photons via upconversion. The energy level structures of Yb^{3+}/Tm^{3+} and the upconversion processes are shown in Fig. 12a. Upon NIR irradiation, the pump photons of 980 nm can excite Yb^{3+} ions, and then the higher energy levels $^3H_5$, $^3F_2$ and $^1G_4$ of Tm^{3+} are populated by three successive energy transfers from Yb^{3+} to Tm^{3+}. Due to the large energy mismatch of ~3516 cm^{-1} in transfer $^2F_{5/2} \rightarrow {}^2F_{7/2}$ (Yb^{3+}): $^1G_4 \rightarrow {}^1D_2$ (Tm^{3+}) between Yb^{3+} and Tm^{3+}, the $^1D_2$ level of Tm^{3+} cannot be populated by the fourth photon from Yb^{3+} by energy transfers to the $^1G_4$ [57]. Hence, the cross relaxation process of $^3F_2 + {}^3H_4 \rightarrow {}^3H_6 + {}^1D_2$ and $^1G_4 + {}^3H_4 \rightarrow {}^3F_4 + {}^1D_2$ between Tm^{3+} ions may be responsible for populating the $^1D_2$ level [7,39]. After that, the state $^1I_6$ level can be populated via the excitation of $^3P_2$ level by another energy transfer process from Yb^{3+} to Tm^{3+} and its nonradiative relaxation to $^1I_6$ level, which can be considered as $^2F_{5/2} \rightarrow {}^2F_{7/2}$ (Yb^{3+}): $^1D_2 \rightarrow {}^1I_6$ (Tm^{3+}) [41,58]. During the decays of high state level, some specific photons may be emitted. As shown in Fig. 12b, the Yb^{3+}/Tm^{3+} codped In_2S_3 exhibts numerous new emission peaks compared to pure In_2S_3 upon excitation at 980 nm. The three emission peaks occured at λ = 295 nm, 344 nm and 370 nm are attributed to the Tm^{3+} transitions of $^1I_6 \rightarrow {}^3H_6$, $^1I_6 \rightarrow {}^3F_4$ and $^1D_2 \rightarrow {}^3H_6$, respectively. The two blue emission peaks centered at λ = 452 nm and 476 nm correspond to $^1D_2 \rightarrow {}^3F_4$ and $^1G_4 \rightarrow {}^3H_6$ transitions of Tm^{3+} ions, respectively. In addition, there are three red emission peaks at λ = 633 nm, 656 nm and 683 nm originating from $^1G_4 \rightarrow {}^3F_4$, $^3F_2 \rightarrow {}^3H_6$ and $^3F_3 \rightarrow {}^3H_6$ transitions of Tm^{3+} ions, respectively [40,58]. These fluorescence emission energy can be further transferred or absorbed by the photocatalyst or pollutants for the photocatalytic reaction through irradiative energy transfer and non – irradiative energy transfer process.

As schemed in Fig. 12c, the Yb^{3+}/Tm^{3+} co – dped In_2S_3 can be excited by the energy transfer of Tm^{3+} to produce the electron (e^-) and hole (h^+) on the conduction band (CB) and valence band (VB), respectively. Due to the presence of intermediate energy states and/or sulfur vacancies, the photogenerated electron can be immediately captured, resulting in the efficient separation rate and low recombination of carriers [44,56]. Those electrons on intermediate energy states and/or sulfur vacancies are futher to get into contact with oxidizing substance for reduction reaction. As the CB edge potential of YTIS-4 is −0.41 V vs NHE, which is more negative than the Cr(VI)/Cr (III) potential (+0.51 V vs NHE), the Cr(VI) can be easily reduced to generate the Cr(III) (Fig. 12c(i)) [59,60]. As for RhB (Fig. 12c(ii)), there is another way to produce electrons. The RhB molecular can be excited to emit electrons by absorbing the transfered photons around λ = 554 nm. The electrons are released and transferred to the CB of Yb^{3+}/Tm^{3+} codped In_2S_3, and then collected by intermediate energy states and/or sulfur vacancies [61]. Due to that the standard redox potential E^0 ($O_2/\cdot O_2^-$) is −0.33 eV *vs* NHE, which is lower than the CB edge potential of −0.41 V vs NHE, the O_2 in the solution can easily accept the photoexcited electron to form the $\cdot O_2^-$ radicals for $RhB^{\bullet+}$ oxidation. Meanwhile, the photogenerated holes (h^+) left behind on the VB of Yb^{3+}/Tm^{3+} codped In_2S_3 could direct oxidize the RhB/$RhB^{\bullet+}$ molecule to small molecules and even carbon dioxide and water [62].

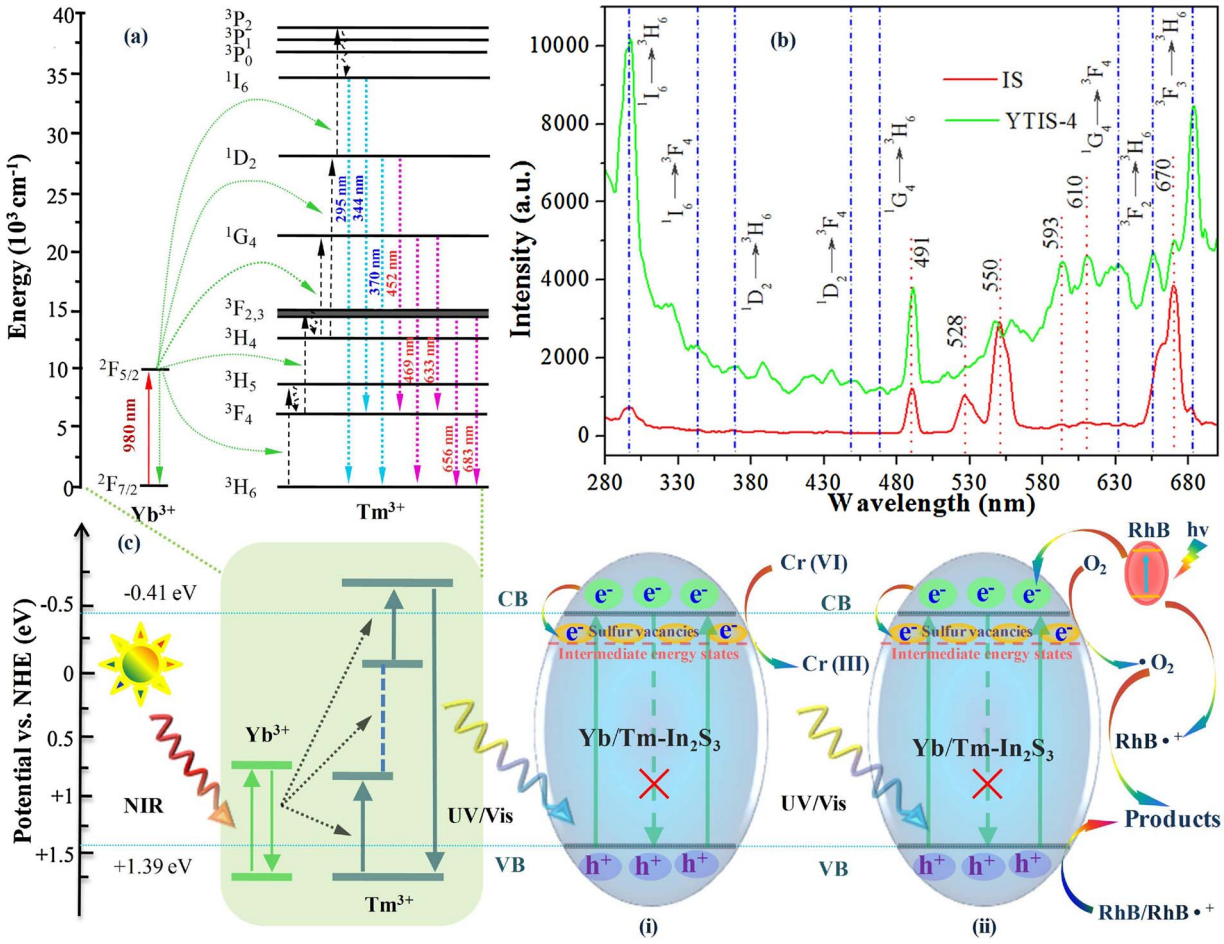

Fig. 12. Schematic diagram of the upconversion processes and energy-level structures of Tm^{3+} and Yb^{3+} ions (a); The upconversion emission spectra of the Yb^{3+}, Tm^{3+} doped In_2S_3 upon excitation at 980 nm (b); (c) Schematic of photocatalytic process of YTIS for Cr (VI) and RhB degradation.

4. Conclusions

The highly photoactive flower−like tetragonal Yb^{3+}/Tm^{3+} co-doped In_2S_3 is synthesized via a facil hydrothermal process. The doping can induce the formation of intermediate energy states with sulfur vacancies for the trapping of photogenerated electrons, and hence improving the carrier separation efficiency and photocatlytic activity. The Yb^{3+}/Tm^{3+} co−doping of In_2S_3 has the synergistic effect on Cr (VI) reduction and RhB degradation compared with individually doped In_2S_3. The YTIS−4 shows the optimum remarkably enhanced photocatalytic performance under the irradiation from UV to NIR light. The photocatalytic rate of YTIS−4 for Cr(VI) reduction (99.4% removal) and RhB degradation (94.8% removal) is 2.17 and 5.60 times than that of pure In_2S_3 under the full−spectra−light illumination for 6 min and 7 min, respectively. The upconversion process via energy level transition of Yb^{3+}/Tm^{3+} provides suitable energy for the activation and subsequent photocatalysis of YTIS under NIR irradiation. The ·O2− and h^+ are the main reactive species for RhB decomposition and the YTIS−4 has an excellent reusability towards Cr(VI) and RhB removal. Therefore, Yb^{3+}/Tm^{3+} codoped In_2S_3 could be an efficient photocatalysts with great application potential in environmental pollutants removal in the overall range of light spectrum.

Conflict fo interests

None.

Acknowledgements

The authors gratefully acknowledge the financial support provided by the Key research and development project of Hunan Province, China (No. 2016SK2015), the National Natural Science Foundation of China (No. 51521006, 51739004, 51378192).

References

[1] L. Shao, D. Jiang, P. Xiao, L. Zhu, S. Meng, M. Chen, Enhancement of g-C_3N_4 nanosheets photocatalysis by synergistic interaction of ZnS microsphere and RGO inducing multistep charge transfer, Appl. Catal. B: Environ. 198 (2016) 200–210.
[2] Z. Wu, X. Yuan, H. Zhong, H. Wang, G. Zeng, X. Chen, H. Wang, L. Zhang, J. Shao, Enhanced adsorptive removal of p-nitrophenol from water by aluminum metal-organic framework/reduced graphene oxide composite, Sci. Rep. 6 (2016) 25638–25651.
[3] Y. Zheng, W. Wang, D. Jiang, L. Zhang, X. Li, Z. Wang, Ultrathin mesoporous Co_3O_4 nanosheets with excellent photo-/thermo-catalytic activity, J. Mater. Chem. A 4 (2016) 105–112.
[4] S. Wang, Y. Guan, L. Wang, W. Zhao, H. He, J. Xiao, S. Yang, C. Sun, Fabrication of a novel bifunctional material of BiOI/Ag_3VO_4 with high adsorption–photocatalysis for efficient treatment of dye wastewater, Appl. Catal. B: Environ. 168–169 (2015) 448–457.
[5] H. Wang, X. Yuan, Y. Wu, G. Zeng, X. Chen, L. Leng, Z. Wu, L. Jiang, H. Li, Facile synthesis of amino-functionalized titanium metal-organic frameworks and their superior visible-light photocatalytic activity for Cr(VI) reduction, J. Hazard. Mater. 286 (2015) 187–194.
[6] M. Zeng, Y. Li, M. Mao, J. Bai, L. Ren, X. Zhao, Synergetic effect between photocatalysis on TiO_2 and thermocatalysis on CeO_2 for gas-Phase oxidation of benzene on TiO_2/CeO_2 nanocomposites, ACS Catal. 5 (2015) 3278–3286.
[7] Y. Tang, W. Di, X. Zhai, R. Yang, W. Qin, NIR-Responsive photocatalytic activity and mechanism of $NaYF_4$:Yb,Tm@TiO_2 Core–Shell nanoparticles, ACS Catal. 3 (2013) 405–412.
[8] F. Liu, M. Zeng, Y. Li, Y. Yang, M. Mao, X. Zhao, UV-Vis-Infrared light driven thermocatalytic activity of octahedral layered birnessite nanoflowers enhanced by a novel photoactivation, Adv. Funct. Mater. 26 (2016) 4518–4526.

[9] J. Hou, Y. Li, M. Mao, Y. Yue, G.N. Greaves, X. Zhao, Full solar spectrum light driven thermocatalysis with extremely high efficiency on nanostructured Ce ion substituted OMS-2 catalyst for VOCs purification, Nanoscale 7 (2015) 2633–2640.

[10] P. Calza, C. Hadjicostas, V.A. Sakkas, M. Sarro, C. Minero, C. Medana, T.A. Albanis, Photocatalytic transformation of the antipsychotic drug risperidone in aqueous media on reduced graphene oxide-TiO_2 composites, Appl. Catal. B: Environ. 183 (2016) 96–106.

[11] L. Ren, M. Mao, Y. Li, L. Lan, Z. Zhang, X. Zhao, Novel photothermocatalytic synergetic effect leads to high catalytic activity and excellent durability of anatase TiO_2 nanosheets with dominant {001} facets for benzene abatement, Appl. Catal. B: Environ. 198 (2016) 303–310.

[12] L. Pan, T. Muhammad, L. Ma, Z.-F. Huang, S. Wang, L. Wang, J.-J. Zou, X. Zhang, MOF-derived C-doped ZnO prepared via a two-step calcination for efficient photocatalysis, Appl. Catal. B: Environ. 189 (2016) 181–191.

[13] K. Vinodgopal, P.V. Kamat, Enhanced rates of photocatalytic degradation of an azo dye using SnO_2/TiO_2 coupled semiconductor thin films, Environ. Sci. Technol. 29 (1995) 841–845.

[14] M. Zeng, Y. Li, F. Liu, Y. Yang, M. Mao, X. Zhao, Cu doped OL-1 nanoflower: a UV?vis-infrared light-driven catalyst for gas-phase environmental purification with very high efficiency, Appl. Catal. B: Environ. 200 (2017) 521–529.

[15] M. Mao, Y. Li, J. Hou, M. Zeng, X. Zhao, Extremely efficient full solar spectrum light driven thermocatalytic activity for the oxidation of VOCs on OMS-2 nanorod catalyst, Appl. Catal. B: Environ. 174–175 (2015) 496–503.

[16] G. Wang, B. Huang, X. Ma, Z. Wang, X. Qin, X. Zhang, Y. Dai, M.H. Whangbo, $Cu_2(OH)PO_4$, a near-infrared-activated photocatalyst, Angew. Chem. Int. Ed. Engl. 52 (2013) 4810–4813.

[17] J. Tian, Y. Sang, G. Yu, H. Jiang, X. Mu, H. Liu, A Bi_2WO_6–based hybrid photocatalyst with broad spectrum photocatalytic properties under UV, visible, and near-infrared irradiation, Adv. Mater. 25 (2013) 5075–5080.

[18] T. Jing, Y. Dai, W. Wei, X. Ma, B. Huang, Near-infrared photocatalytic activity induced by intrinsic defects in Bi_2MO_6 (M = W, Mo), Phys. Chem. Chem. Phys. 16 (2014) 18596–18604.

[19] Y. Sang, Z. Zhao, M. Zhao, P. Hao, Y. Leng, H. Liu, From UV to near-infrared, WS_2 nanosheet: a novel photocatalyst for full solar light spectrum photodegradation, Adv. Mater. 27 (2015) 363–369.

[20] W. Gao, W. Liu, Y. Leng, X. Wang, X. Wang, B. Hu, D. Yu, Y. Sang, H. Liu, In_2S_3 nanomaterial as a broadband spectrum photocatalyst to display significant activity, Appl. Catal. B: Environ. 176–177 (2015) 83–90.

[21] Z. Wu, X. Yuan, H. Wang, Z. Wu, L. Jiang, H. Wang, L. Zhang, Z. Xiao, X. Chen, G. Zeng, Facile synthesis of a novel full-spectrum-responsive $Co_{2.67}S_4$ nanoparticles for UV-, vis- and NIR-driven photocatalysis, Appl. Catal. B: Environ. 202 (2017) 104–111.

[22] X. Zhang, L. Yu, C. Zhuang, T. Peng, R. Li, X. Li, Highly asymmetric phthalocyanine as a sensitizer of graphitic carbon nitride for extremely efficient photocatalytic H_2 production under near-Infrared light, ACS Catal. 4 (2014) 162–170.

[23] H. Li, R. Liu, Y. Liu, H. Huang, H. Yu, H. Ming, S. Lian, S.-T. Lee, Z. Kang, Carbon quantum dots/Cu_2O composites with protruding nanostructures and their highly efficient (near) infrared photocatalytic behavior, J. Mater. Chem. 22 (2012) 17470.

[24] Z.W. Seh, S. Liu, M. Low, S.Y. Zhang, Z. Liu, A. Mlayah, M.Y. Han, Janus Au-TiO_2 photocatalysts with strong localization of plasmonic near-fields for efficient visible-light hydrogen generation, Adv. Mater. 24 (2012) 2310–2314.

[25] A.D. Liyanage, S.D. Perera, K. Tan, Y. Chabal, K.J. Balkus, Synthesis, characterization, and photocatalytic activity of Y-Doped CeO_2 nanorods, ACS Catal. 4 (2014) 577–584.

[26] J. Fang, D. Li, Y. Shao, J. Hu, Unusual photocatalytic materials with UV-VIS-NIR spectral response: deciphering the photothermocatalytic synergetic effect of Pt/$LaVO_4$/TiO_2, J. Mater. Chem. A 4 (2016) 14213–14221.

[27] X. Yuan, H. Wang, Y. Wu, X. Chen, G. Zeng, L. Leng, C. Zhang, A novel SnS_2–$MgFe_2O_4$/reduced graphene oxide flower-like photocatalyst: solvothermal synthesis, characterization and improved visible-light photocatalytic activity, Catal. Commun. 61 (2015) 62–66.

[28] H. Wang, X. Yuan, H. Wang, X. Chen, Z. Wu, L. Jiang, W. Xiong, G. Zeng, Facile synthesis of Sb_2S_3/ultrathin g-C_3N_4 sheets heterostructures embedded with g-C_3N_4 quantum dots with enhanced NIR-light photocatalytic performance, Appl. Catal. B: Environ. 193 (2016) 36–46.

[29] L. Jiang, X. Yuan, Y. Pan, J. Liang, G. Zeng, Z. Wu, H. Wang, Doping of graphitic carbon nitride for photocatalysis: a reveiw, Appl. Catal. B: Environ. 217 (2017) 388–406.

[30] J. Chen, W. Liu, W. Gao, Tuning photocatalytic activity of In_2S_3 broadband spectrum photocatalyst based on morphology, Appl. Surf. Sci. 368 (2016) 288–297.

[31] Y. Li, T. Li, J. Tian, X. Wang, H. Cui, TiO_2 nanobelts decorated with In_2S_3 nanoparticles as photocatalysts with enhanced full-Solar-Spectrum (UV-vis-NIR) photocatalytic activity toward the degradation of tetracycline, Part. Part. Syst. Char. (2017) 1700127.

[32] H. Wang, X. Yuan, Y. Wu, G. Zeng, H. Dong, X. Chen, L. Leng, Z. Wu, L. Peng, In situ synthesis of In_2S_3@MIL-125(Ti) core–shell microparticle for the removal of tetracycline from wastewater by integrated adsorption and visible-light-driven photocatalysis, Appl. Catal. B: Environ. 186 (2016) 19–29.

[33] R. Adhikari, G. Gyawali, S.H. Cho, R. Narro-García, T. Sekino, S.W. Lee, Er^{3+}/Yb^{3+} co-doped bismuth molybdate nanosheets upconversion photocatalyst with enhanced photocatalytic activity, J. Solid State Chem. 209 (2014) 74–81.

[34] Y. Liu, G. Zhu, J. Gao, R. Zhu, M. Hojamberdiev, C. Wang, X. Wei, P. Liu, A novel synergy of Er^{3+}/Fe^{3+} co-doped porous Bi_5O_7I microspheres with enhanced photocatalytic activity under visible-light irradiation, Appl. Catal. B: Environ. 205 (2017) 421–432.

[35] S. Zhuo, M. Shao, S.T. Lee, Upconversion and downconversion fluorescent graphene quantum dots: ultrasonic preparation and photocatalysis, ACS Nano 6 (2012) 1059–1064.

[36] X. Li, H. Ren, Z. Zou, J. Sun, J. Wang, Z. Liu, Energy gap engineering of polymeric carbon nitride nanosheets for matching with NaYF4:Yb,Tm: enhanced visible-near infrared photocatalytic activity, Chem. Commun. 52 (2016) 453–456.

[37] W. Qin, D. Zhang, D. Zhao, L. Wang, K. Zheng, Near-infrared photocatalysis based on YF_3:Yb^{3+}, Tm^{3+}/TiO_2 core/shell nanoparticles, Chem. Commun. 46 (2010) 2304–2306.

[38] S. Obregon, A. Kubacka, M. Fernandez-Garcia, G. Colon, High-performance Er^{3+}–TiO^2 system: dual up-conversion and electronic role of the lanthanide, J. Catal. 299 (2013) 298–306.

[39] W. Wang, Y. Li, Z. Kang, F. Wang, J.C. Yu, A NIR-driven photocatalyst based on α-$NaYF_4$:Yb,Tm@TiO_2 core–shell structure supported on reduced graphene oxide, Appl. Catal. B: Environ. 182 (2016) 184–192.

[40] F. Zhang, C.L. Zhang, W.N. Wang, H.P. Cong, H.S. Qian, Titanium Dioxide/Upconversion Nanoparticles/Cadmium sulfide nanofibers enable enhanced full-Spectrum absorption for superior solar light driven photocatalysis, ChemSusChem 9 (2016) 1449–1454.

[41] X. Guo, W. Di, C. Chen, C. Liu, X. Wang, W. Qin, Enhanced near-infrared photocatalysis of NaYF4:Yb, Tm/CdS/TiO_2 composites, Dalton Trans. 43 (2014) 1048–1054.

[42] S. Huang, Z. Lou, Z. Qi, N. Zhu, H. Yuan, Enhancing upconversion emissions of Er^{3+}/Tm^{3+}/Yb^{3+} tridoped ($NaY(WO_4)_2$/YF_3) through TiO_2 coating and Bi^{3+} doping and its photocatalytic applications, Appl. Catal. B: Environ. 168–169 (2015) 313–321.

[43] T. Liu, G. Tan, C. Zhao, C. Xu, Y. Su, Y. Wang, H. Ren, A. Xia, D. Shao, S. Yan, Enhanced photocatalytic mechanism of the Nd-Er co-doped tetragonal $BiVO_4$ photocatalysts, Appl. Catal. B: Environ. 213 (2017) 87–96.

[44] S. Obregón, G. Colón, Excellent photocatalytic activity of Yb^{3+} Er^{3+} co-doped $BiVO_4$ photocatalyst, Appl. Catal. B: Environ. 152–153 (2014) 328–334.

[45] S. Ganguli, C. Hazra, M. Chatti, T. Samanta, V. Mahalingam, A highly efficient UV-Vis-NIR active Ln(3 +)-Doped $BiPO_4$/$BiVO_4$ nanocomposite for photocatalysis application, Langmuir 32 (2016) 247–253.

[46] C. Regmi, Y.K. Kshetri, S.K. Ray, R.P. Pandey, S.W. Lee, Utilization of visible to NIR light energy by Yb^{+3}, Er^{+3} and Tm^{+3} doped $BiVO_4$ for the photocatalytic degradation of methylene blue, Appl. Surf. Sci. 392 (2017) 61–70.

[47] J. Zhang, Y. Huang, L. Jin, F. Rosei, F. Vetrone, J.P. Claverie, Efficient upconverting multiferroic Core@Shell photocatalysts: visible-to-Near-Infrared photon harvesting, ACS Appl. Mater. Interfaces 9 (2017) 8142–8150.

[48] Y. Cheng, H. Niu, J. Chen, J. Song, C. Mao, S. Zhang, C. Chen, Y. Gao, Highly stable hierarchical flower-like β-In_2S_3 assembled from 2D nanosheets with high adsorption-Photodecolorization activities for the treatment of wastewater, J. Nanopart. Res. 19 (2017).

[49] T. Xu, L. Zhang, H. Cheng, Y. Zhu, Significantly enhanced photocatalytic performance of ZnO via graphene hybridization and the mechanism study, Appl. Catal. B: Environ. 101 (2011) 382–387.

[50] E. Gao, W. Wang, M. Shang, J. Xu, Synthesis and enhanced photocatalytic performance of graphene-Bi_2WO_6 composite, Phys. Chem. Chem. Phys. 13 (2011) 2887–2893.

[51] X. Gao, Z. Wang, X. Zhai, F. Fu, W. Li, The synthesize of lanthanide doped $BiVO_4$ and its enhanced photocatalytic activity, J. Mol. Liq. 211 (2015) 25–30.

[52] L. Jiang, X. Yuan, G. Zeng, X. Chen, Z. Wu, J. Liang, J. Zhang, H. Wang, H. Wang, Phosphorus- and sulfur-Codoped g-C_3N_4: facile preparation, mechanism insight, and application as efficient photocatalyst for tetracycline and methyl orange degradation under visible light irradiation, ACS Sustain Chem. Eng. 5 (2017) 5831–5841.

[53] J. Zhang, X. Yuan, L. Jiang, Z. Wu, X. Chen, H. Wang, H. Wang, G. Zeng, Highly efficient photocatalysis toward tetracycline of Nitrogen Doped carbon quantum Dots sensitized Bi_2WO_6 based on interfacial charge transfer, J. Colloid Interf. Sci. 511 (2018) 296–306.

[54] Z. Wu, X. Yuan, J. Zhang, H. Wang, L. Jiang, G. Zeng, Photocatalytic decontamination of wastewater containing organic dyes by metal-organic frameworks and their derivatives, ChemCatChem 9 (2017) 41–64.

[55] H. Wang, X. Yuan, Y. Wu, X. Chen, L. Leng, H. Wang, H. Li, G. Zeng, Facile synthesis of polypyrrole decorated reduced graphene oxide–Fe_3O_4 magnetic composites and its application for the Cr(VI) removal, Chem. Eng. J. 262 (2015) 597–606.

[56] S. Hu, Y. Li, F. Li, Z. Fan, H. Ma, W. Li, X. Kang, Construction of g-C_3N_4/$Zn_{0.11}Sn_{0.12}Cd_{0.88}S_{1.12}$Hybrid heterojunction catalyst with outstanding nitrogen photofixation performance induced by sulfur vacancies, ACS Sustain Chem. Eng. 4 (2016) 2269–2278.

[57] G. Qin, W. Qin, C. Wu, S. Huang, J. Zhang, S. Lu, D. Zhao, H. Liu, Enhancement of ultraviolet upconversion in Yb^{3+} and Tm^{3+} codoped amorphous fluoride film prepared by pulsed laser deposition, J. Appl. Phys. 93 (2003) 4328–4330.

[58] X. Chen, Z. Song, Study on six-photon and five-photon ultraviolet upconversion luminescence, J. Opt. Soc. Am. B 24 (2007) 965.

[59] R. Liang, L. Shen, F. Jing, N. Qin, L. Wu, Preparation of MIL-53(Fe)-Reduced graphene oxide nanocomposites by a simple self-Assembly strategy for increasing interfacial contact: efficient visible-Light photocatalysts, ACS Appl. Mater. Interfaces 7 (2015) 9507–9515.

[60] Z. Wu, X. Yuan, H. Zhong, H. Wang, L. Jiang, G. Zeng, H. Wang, Z. Liu, Y. Li, Highly efficient adsorption of Congo red in single and binary water with cationic dyes by reduced graphene oxide decorated NH_2 −MIL-68(Al), J. Mol. Liq. 247 (2017) 215–229.

[61] H. Wang, X. Yuan, Y. Wu, G. Zeng, X. Chen, L. Leng, H. Li, Synthesis and applications of novel graphitic carbon nitride/metal-organic frameworks mesoporous photocatalyst for dyes removal, Appl. Catal. B: Environ. 174–175 (2015) 445–454.

[62] L. Jiang, X. Yuan, G. Zeng, Z. Wu, J. Liang, X. Chen, L. Leng, H. Wang, H. Wang, Metal-free efficient photocatalyst for stable visible-light photocatalytic degradation of refractory pollutant, Appl. Catal. B: Environ. 221 (2018) 715–725.